Near-Inertial Mixing in the Central Arctic Ocean

ILKER FER

Geophysical Institute, University of Bergen, Bergen, Norway

(Manuscript received 4 June 2013, in final form 19 February 2014)

ABSTRACT

Observations were made in April 2007 of horizontal currents, hydrography, and shear microstructure in the upper 500 m from a drifting ice camp in the central Arctic Ocean. An approximately 4-day-long time series, collected about 10 days after a storm event, shows enhanced near-inertial oscillations in the first half of the measurement period with comparable upward- and downward-propagating energy. Rough estimates of wind work and near-inertial flux imply that the waves were likely generated by the previous storm. The near-inertial frequency band is associated with dominant clockwise rotation in time of the horizontal currents and enhanced dissipation rates of turbulent kinetic energy. The vertical profile of dissipation rate shows elevated values in the pycnocline between the relatively turbulent underice boundary layer and the deeper quiescent water column. Dissipation averaged in the pycnocline is near-inertially modulated, and its magnitude decays approximately at a rate implied by the reduction of energy over time. Observations suggest that near-inertial energy and internal wave–induced mixing play a significant role in vertical mixing in the Arctic Ocean.

1. Introduction

Back-of-the-envelope calculations show that there is enough heat in the Atlantic layer in the Arctic Ocean to melt the entire Arctic ice cover in four years, provided that all the heat reached the surface under the ice pack (Turner 2010). The strongly stratified cold halocline layer (CHL) of the Arctic Ocean is an efficient barrier for the vertical exchange of this heat (Fer 2009). Dramatically decreasing ice cover (Comiso 2012; Stroeve et al. 2012), however, may lead to increased vertical mixing by allowing more wind energy into the ocean.

Near-inertial waves, those slightly above the inertial frequency, develop as a response to impulsive atmospheric forcing, such as storms, and are constrained to refract equatorward. While a substantial portion of the wind energy can directly mix the upper mixed layer, a fraction can propagate deeper into the water column as near-inertial waves, contributing to deeper vertical mixing provided that the waves break (Alford 2010). Near-inertial internal waves typically dominate the energetics of the internal wave field both in mid- and low latitudes (see, e.g., D'Asaro and Perkins 1984; Alford and Gregg 2001; Alford et al. 2012) and in the Arctic Ocean (D'Asaro and Morehead 1991; Halle and Pinkel 2003; Pinkel 2005). During the 1997/98 Surface Heat Balance of the Arctic Ocean (SHEBA) drift, velocity measurements showed downward-propagating near-inertial waves dominating the superinertial motion field (Pinkel 2005).

Historically, the internal wave field in the Arctic Ocean, particularly in the central basins, is remarkably less energetic than the lower-latitude open ocean (Levine et al. 1985, 1987). The presence of ice impedes the input of energy into the ocean (Rainville and Woodgate 2009) and increases the dissipation of internal wave energy (Morison et al. 1985). Dissipation in the underice boundary appears to be a dominant mechanism of internal wave energy loss where the energy following a single round trip to the seafloor is substantially absorbed, leading to a single bounce rather than a trans-Arctic propagation (Pinkel 2005). While wind-driven near-inertial motion is more common in summer when the ice pack is relatively loose (Plueddemann et al. 1998; Rainville and Woodgate 2009), there have been indications of enhanced near-inertial motion in winter (Merrifield and Pinkel 1996) and in early winter, after the freeze up (Halle and Pinkel 2003).

The rapid retreat and thinning of the Arctic sea ice cover (Kwok and Rothrock 2009; Comiso 2012; Stroeve et al. 2012) suggests that the internal wave field in the Arctic can be energized through more input of wind and near-inertial energy. The effect of decreasing ice cover on the internal wave energetics, however, is not

Corresponding author address: Ilker Fer, Geophysical Institute, University of Bergen, Allégaten 70, 5007 Bergen, Norway.
E-mail: ilker.fer@gfi.uib.no

DOI: 10.1175/JPO-D-13-0133.1

well established. Observations from the Chukchi shelf show enhanced near-inertial wave energy and shear (and inferred vertical mixing) during ice-free conditions (Rainville and Woodgate 2009). The water is shallow (70 m), and the observations may not be representative of the internal wave propagation or sea ice dynamics in the deep Arctic. Comparisons of internal wave energy between modern and historical data, reanalyzed in identical fashion, reveal no evident trend over a 30-yr period in spite of drastic diminution of the sea ice (Guthrie et al. 2013). Guthrie et al. (2013) attribute this to the increased upper-layer stratification by meltwater that increases the boundary layer dissipation of internal wave energy.

The fraction of the near-inertial energy flux penetrating deep into the ocean and contributing to mixing is uncertain. Mid- and low-latitude studies in the open ocean indicate that a large fraction of the near-inertial energy is dissipated in the upper ocean and the remaining energy can propagate into the deep ocean. D'Asaro et al. (1995) found that the depth-integrated energy input by a storm in the northeast Pacific Ocean decreased by 36% (±10%) after 3 weeks, suggesting that a fraction of the near-inertial energy propagated away from the study site. A numerical study by Furuichi et al. (2008) indicates that 85% of the near-inertial energy input into the mixed layer is dissipated in the upper 150 m. The two years of observations at Ocean Station Papa show that a substantial fraction of the energy input into the mixed layer, about 12%–33% of the wind work, reaches the deep sea (Alford et al. 2012). If the midlatitude observations are applicable to the Arctic Ocean, the near-inertial energy can contribute significantly to mixing the CHL (typically shallower than 150 m) and may also play a role in mixing the deep Arctic. Even though the internal wave energy is low in the Arctic Ocean, its variability is dominated by the near-inertial band, similar to the open ocean.

Observations are presented here of currents, hydrography, and microstructure collected during the drift of the Barneo ice camp (approximately 89°N; Fig. 1) in April 2007. (The camp is called Borneo in some publications.) The measurements were made approximately 10 days after a storm event that led to significant ice deformation and damaged the landing strip. The microstructure data from this survey were previously reported in Fer (2009), with focus on mixing across the CHL: survey-mean profiles and the structure of turbulent parameters and the vertical heat flux across the CHL were presented. In this paper, the near-inertial frequency band motions that appear in shear and strain and their influence on turbulent mixing in the upper 300 m are discussed. Rough estimates of wind work and near-inertial energy flux imply that the waves were likely generated by the previous storm. The dissipation rate of turbulent kinetic energy, averaged in the pycnocline, is

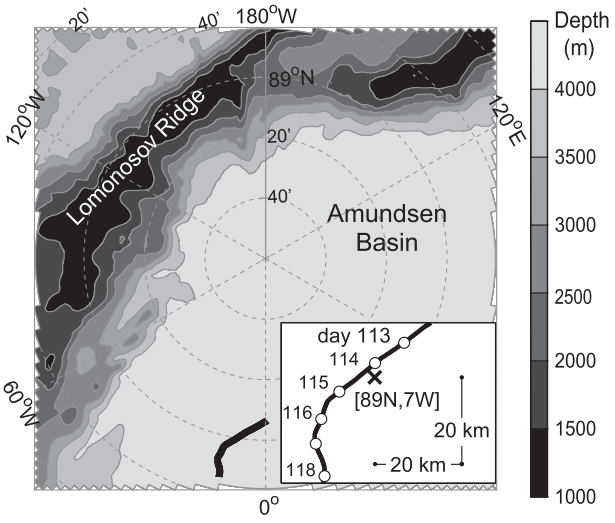

FIG. 1. Drift track of the Barneo ice camp (thick black curve), superimposed on the International Bathymetric Chart of the Arctic Ocean (IBCAO) bathymetry (isobaths every 500 m). The inset is a blowup of the drift. Circles are placed at daily intervals, at start of each day of year. The distance in km is referenced to 89°N, 7°W (marked by the X).

near-inertially modulated, and its magnitude decays approximately at a rate implied by the reduction of energy over time. Our observations and analysis suggest that the dissipation of near-inertial wave energy can play a significant role in mixing in the upper layers of the Arctic Ocean.

2. Experiment description

Finescale velocity and microstructure profiles were collected between 24 and 30 April 2007 from the Barneo ice camp, about 110 km from the North Pole (Fig. 1). The water depth at the site is 4300 m. Microstructure measurements were made by a loosely tethered free-fall profiler. Current profiles were obtained using an acoustic Doppler current profiler (ADCP) as well as expendable current profilers (XCPs). The details of each instrument and the corresponding sampling scheme are described below. GPS fixes were obtained every second from a Magellan differential GPS (DGPS3011). In the following, time is given as decimal day of year 2007; 25 April at noon is day 114.5.

a. Microstructure profiling

The microstructure profiler used was an MSS90L, manufactured by ISW Wassermesstechnik (Germany). Deployment methods and data processing are described in Fer (2009). The entire experiment was conducted by the author alone; hence, the time series was interrupted by about 9 h of rest between 15-h duration sampling sets. In total, 100 microstructure profiles were collected in five 15-h sets, at

a frequency of about one cast every 50 min. Data (downcasts only) were recorded from immediately below the ice to typically 500-m depth. Profiles of dissipation rate of turbulent kinetic energy (TKE) per unit mass ε are computed using the isotropic formula and shear variance obtained from spectral analysis of 1-s segments of shear probe signal. The lowest detection level of ε is $(5 - 7) \times 10^{-10}$-$\mathrm{W\,kg^{-1}}$. Profiles are averaged vertically in 1-m bins. The diapycnal eddy diffusivity is calculated as $K_\rho = 0.2\varepsilon N^{-2}$ (Osborn 1980), using the buoyancy frequency $N = [-(g/\rho_0)\partial\rho/\partial z]^{1/2}$, where ρ is the observed density profile. In calculations of K_ρ, N is computed from the sorted potential density, σ_θ profiles using a reference density of $\rho_0 = 1027\,\mathrm{kg\,m^{-3}}$, and over a 4-m vertical length scale. The term K_ρ is ill defined in the absence of stratification, and we exclude the segments with weak stratification identified as $N < 1.7 \times 10^{-3}\,\mathrm{s^{-1}}$, equivalent to 1 cycle per hour (cph). Note that the vertical resolution (1 m) and the vertical length scale over which density gradient is calculated (4 m) are different than those used in the calculations of shear and Richardson number that were set by the coarse vertical resolution and smoothing of the current profiler (section 4c).

An index for turbulent activity I_A (the so-called buoyancy Reynolds number) is computed as $I_A = \varepsilon/(\nu N^2)$. For low values of I_A, typically less than about 20, neither a net buoyancy flux (i.e., mixing) nor local isotropy is expected (Yamazaki and Osborn 1990). The term I_A can be interpreted as a scaled version of the eddy diffusivity, $I_A \sim (3 \times 10^6)\,K_\rho$, using viscosity $\nu = 1.7 \times 10^{-6}\,\mathrm{m^2\,s^{-1}}$ for cold water.

b. Current profiling

Time series of finescale velocity were collected using a downward-looking 75-kHz Longranger RD Instruments ADCP. The ADCP was mounted on a frame and suspended with transducers just beneath the ice, fixed with respect to azimuth. The instrument sampled velocity profiles at 3-s intervals in 8-m-thick cells with the first cell centered at about 13 m. Data recorded in beam coordinates were referenced to geographic north using time series of precise differential global positioning satellite (DGPS) measurements of the local ice orientation. Absolute water velocity was obtained by adding the DGPS-derived ice velocity vector to the relative velocity profile. For the analysis, the velocity profiles were averaged in 1-h intervals (see section 4a for justification of the choice of temporal averaging). The range of the ADCP was only 450 m because of the low concentration of acoustic scatterers in the Arctic Ocean. Current profiles were recovered between 2250 UTC 25 April and 0945 UTC 29 April.

Additionally, nine XCPs were deployed; three malfunctioned and six returned profiles down to 1800 m.

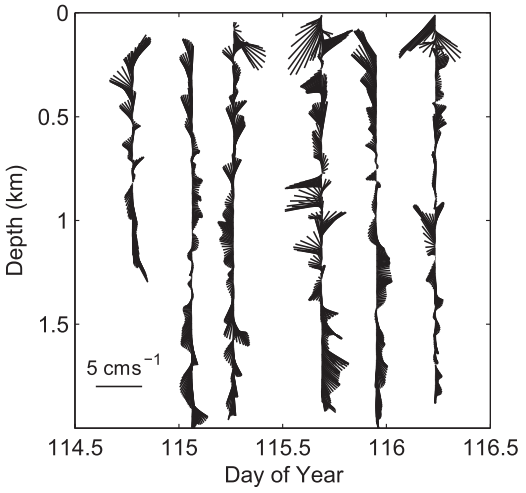

FIG. 2. Horizontal velocity vector profiles, referenced to the depth mean, inferred from the XCP drops. The scale is indicated on the bottom left. In this presentation the vectors are plotted every 5 m after the 1-m vertical resolution profiles are 50-m low-pass filtered.

The XCP measures water velocity relative to a depth-independent mean (error typically less than $1\,\mathrm{cm\,s^{-1}}$) by measuring the voltage induced by the motion of the conducting seawater through Earth's magnetic field (Sanford et al. 1993). Depth is inferred from the time of the fall and a known fall rate. The vertical resolution of a raw profile is about 0.4 m. XCP velocity measurement depends on the nonzero amplitude of the vertical component of the magnetic field, which is large at high latitudes; however, compass errors due to the decreasing size of the horizontal component of the magnetic field result in increasing errors in velocity direction as the magnetic pole is approached. Nevertheless, they have been used successfully at Arctic latitudes (e.g., D'Asaro and Morison 1992; Guthrie et al. 2013). The profiles are processed using 2-m-long moving segments and averaged 1 m vertically, using the data processing package developed at the Applied Physical Laboratory, University of Washington. The velocity profiles are made absolute using the depth-averaged velocity at the time of each XCP cast, measured by the ADCP. Horizontal velocity profiles measured by the XCPs show peak-to-peak fluctuations reaching $5\,\mathrm{cm\,s^{-1}}$ and variability at high vertical modes (Fig. 2).

3. Environmental conditions

A North Pole Environmental Observatory (NPEO; http://psc.apl.washington.edu/northpole) buoy was deployed on the same ice floe, approximately 250 m away from the location of the microstructure profiling. The wind speed

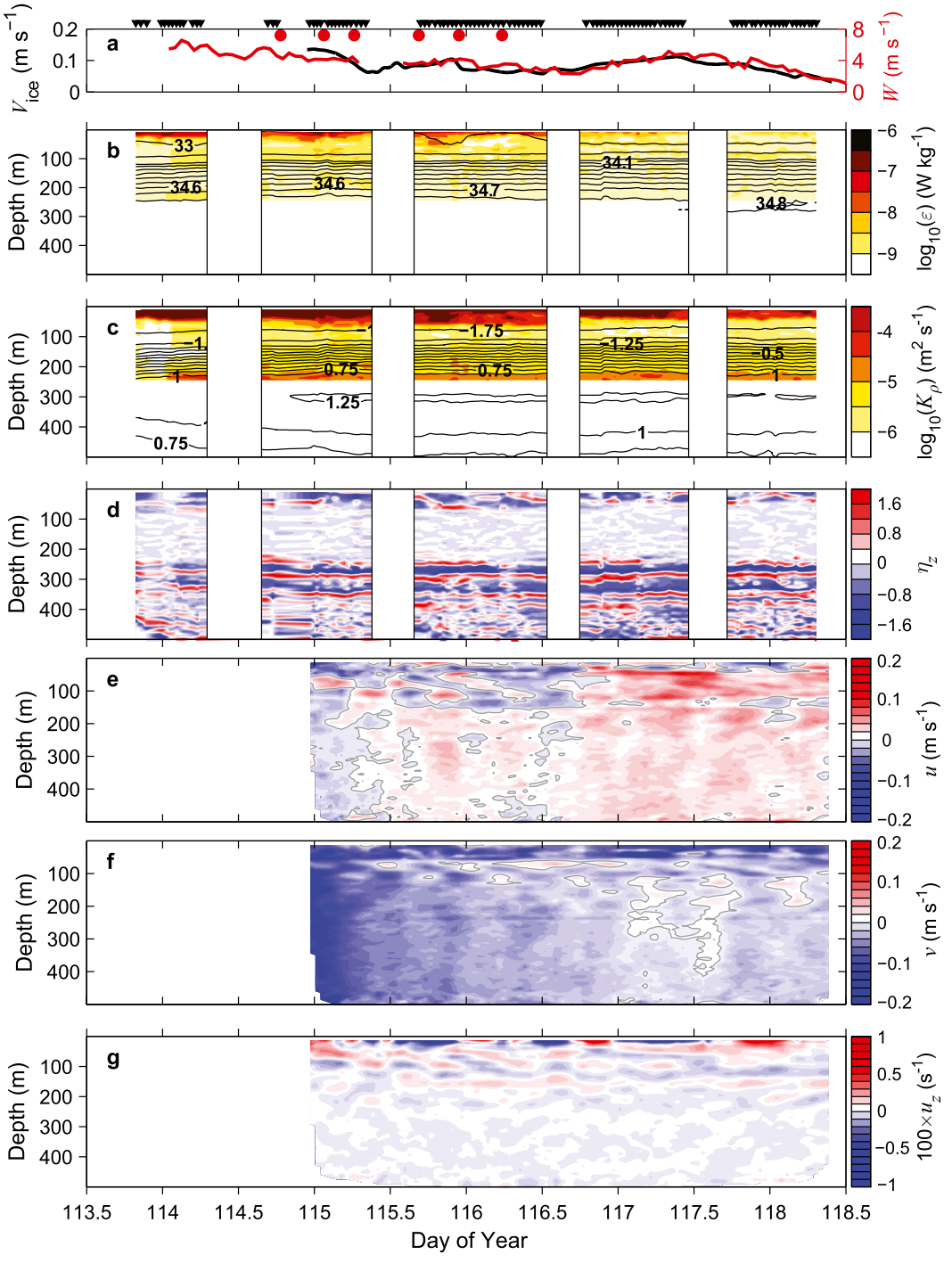

FIG. 3. (a) Time series of ice speed V_{ice} (black), inferred from GPS fixes, and wind speed W, measured by the NPEO buoy (red). Arrowheads on top show the time of microstructure profiles and red circles mark the time of XCP drops. Depth–time contours of (b) dissipation rate ε (color) and salinity S (black contours drawn for $S = 33$, 33.5, 34, and at 0.1 intervals thereafter), (c) eddy diffusivity K_ρ (color) and temperature (black contours at 0.25°C intervals), (d) strain η_z, (e) east u and (f) north v components of horizontal velocity with the gray contour for $u = v = 0$, and (f) zonal shear u_z. In panels (b) and (c), ε and K_ρ are masked below 250-m depth, where ε is at the noise level.

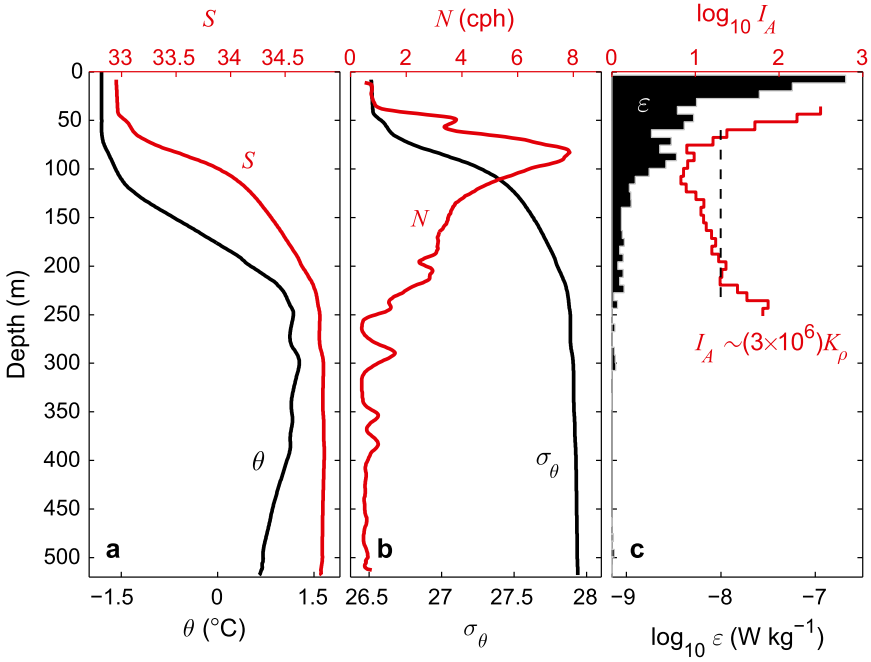

FIG. 4. Survey-averaged profiles of (a) potential temperature θ (black) and salinity S (red), (b) potential density anomaly σ_θ (black) and buoyancy frequency N (red), and (c) logarithm of dissipation rate of TKE ε (black shading) and logarithm of turbulent activity index I_A (red). The thermohaline staircase observed between 200 and 250 m is smeared out because of averaging. Assuming a constant mixing efficiency and molecular viscosity, I_A is a scaled version of the eddy diffusivity: $I_A \sim (3 \times 10^6)K_\rho$. The lower x axis limit for ε is truncated at the noise level of 7×10^{-10} W kg^{-1}. The vertical dashed line in (c) is $I_A = 20$, the approximate threshold below which the diapycnal mixing cannot occur.

measured by the NPEO buoy varied between 1.5 and 7 m s^{-1} with an average of 4 m s^{-1}. The ice drift velocity, inferred from the 1-min-averaged GPS fixes obtained every 1 s, varied coherently with the wind (Fig. 3). The mean drift was 12 cm s^{-1} southwestward near the prime meridian (Fig. 1). The ice thickness was approximately 2 m.

The time–depth evolution of the hydrography, turbulence, and currents during the experiment is shown in Fig. 3. The temperature and salinity structure, with approximately flat isolines, did not change significantly during the drift. Early in the drift the current was relatively strong, between 10 and 20 cm s^{-1} in the entire (ensonified) water column. Slanted phase lines can be seen embedded in this mean flow, particularly in the eastward component of velocity in the first half of the drift. The currents gradually weakened below 100 m. Shear (vertical gradient of horizontal velocity) and strain (vertical gradient of isopycnal displacements; see section 4c) show alternating slanted bands of elevated positive and negative values in the upper part of the water column. In section 5, this variability is attributed to near-inertial motions. The elevated levels of relatively horizontal banded strain below 250 m are because of the strong density gradients associated with a thermohaline staircase.

The survey-averaged profiles from the microstructure profiler are shown in Fig. 4. The hydrography during the time of the measurements was characterized by an upper mixed layer of 38 m, overlaying the cold halocline down to 80 m, followed by the permanent pycnocline and Atlantic-derived water with $\theta > 0$°C below 180 m. Two temperature maxima were recorded, in all microstructure casts, at about 250 and 300 m, separated by a well-mixed 50-m-thick layer. Above the deep temperature maximum, a thermohaline staircase was observed between 200 and 250 m, very similar to that reported in Sirevaag and Fer (2012), close to the same site, during the drift of Barneo 1 yr later in 2008. Dissipation rate decayed with distance from the ice to about 10^{-9} W kg^{-1} at about 100 m, was relatively constant down to about 250 m and then reached the noise level of the instrument. Both the finescale current shear and dissipation were enhanced between 50 and 100 m; however, below the cold halocline and down to 250 m, the turbulent activity index I_A was not significantly above 20. At such low values of I_A, local isotropy is suspect, and turbulence is not sufficiently energetic to generate vertical mixing.

4. Methods

a. ADCP resolution, noise, and time averaging

The quality of ADCP measurements is degraded by the lack of scatterers in the water column, vertical resolution, and the lateral separation of the sonar beams with distance from the transducer. The frequency spectrum of velocity and the vertical wavenumber spectrum of shear from the present dataset are shown in Fig. 5. The spectra are calculated over 32 vertical levels below the surface mixed layer, between 50 and 300 m, where the signal was above the noise levels. The local inertial frequency at 88.9°N is $1.4581 \times 10^{-4}\,\mathrm{s}^{-1}$ (≡0.0835 cph). The frequency spectrum obtained from 10-min time-averaged profiles (i.e., 200 profiles at 3-s intervals) shows a substantial peak near the inertial frequency f, decaying to a white noise level of about $9 \times 10^{-3}\,\mathrm{m\,s}^{-1}$, at a frequency of approximately 1 cph. This noise level is comparable to the statistical uncertainty of approximately $5 \times 10^{-3}\,\mathrm{m\,s}^{-1}$ obtained using averaging over 200 statistically independent profiles with single ping random error of $7.6 \times 10^{-2}\,\mathrm{m\,s}^{-1}$.

The shear spectrum is obtained by dividing the velocity spectrum by $(2\pi m)^2$, where m is the vertical wavenumber in cycles per meter (cpm). Therefore, the white velocity noise appears as a m^2 dependence for shear spectrum (Fig. 5b).

The velocity measurements from Doppler profilers are averages over the length of the transmitted pulse and the vertical bin size of averaging, each set to $\Delta z = 8$ m here. The net effect is a convolution of the true velocity profile with a Bartlett (triangular window) filter with a length of $2\Delta z$. The corresponding spectral transfer function in the vertical wavenumber domain, for finite spatial extent of pulse and range smoothing of the ADCP is $\mathrm{sinc}(\Delta z m)^4$ (Alford and Gregg 2001; Polzin et al. 2002). Shear wavenumber spectra corrected by this transfer function are contrasted with the original spectra in Fig. 5b. To be consistent, the shear noise spectrum (m^2 power law) is also corrected using the same transfer function; hence, it does not appear linear in log–log space. The smoothing by the ADCP's resolution is substantial at high wavenumbers where the noise also starts to dominate the spectra. The effect of the choice of time averaging interval is illustrated following Alford and Gregg (2001), where a model shear noise spectrum scales inversely with the averaging time interval. A 10-min averaging interval reaches the noise level at a vertical scale of about 50 m. By using hourly averages, relatively noise free spectrum is obtained to about $m = 0.04$ cpm, that is, approximately 25-m vertical scale. We base our following analysis on hourly averages of ADCP data and wavenumbers lower than $m = 0.04$ cpm and use a vertical scale of 24 m (i.e., every fourth vertical measurement point of the ADCP) in calculations of vertical gradients. The noise level for the shear variance, obtained by integrating the 1-h noise spectrum for length scales larger than 24 m is approximately $10^{-6}\,\mathrm{s}^{-2}$. To be consistent with shear calculations, the 24-m vertical scale is used in $N(z)$ and strain calculations (section 4c).

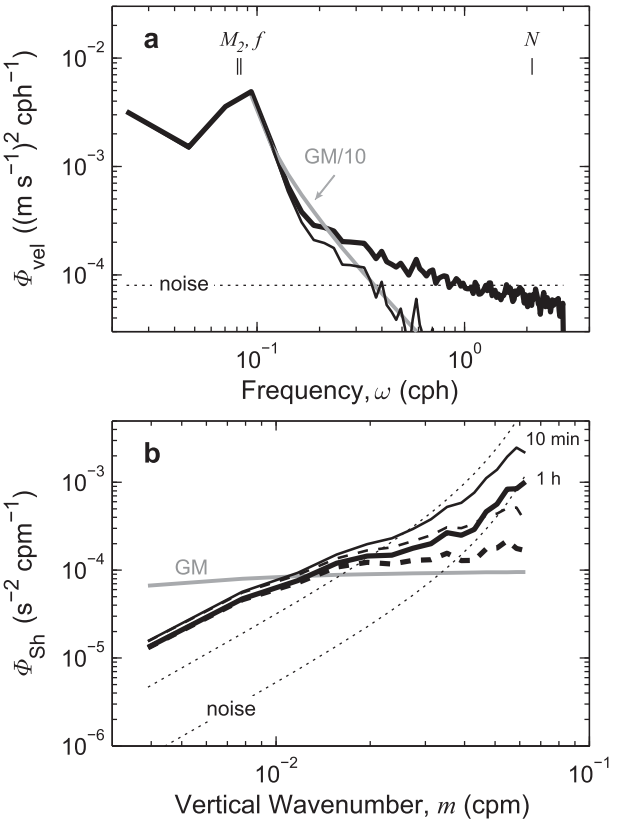

FIG. 5. (a) Velocity frequency spectrum from the ADCP using 10-min-averaged time series (thick is observed; thin is noise removed). Spectra from 32 levels between 50- and 300-m depth are averaged. (b) Vertical wavenumber spectrum for shear calculated between 50- and 300-m depth (FFT length is 32) using 10-min-averaged (thin) and hourly averaged (thick) velocity profiles. Solid curves are the shear spectra corrected for the resolution and range smoothing of the ADCP. To be consistent, the shear noise spectrum (m^2 power law) is also corrected using the same transfer function. In each panel, the corresponding GM spectrum (Garrett and Munk 1975; Cairns and Williams 1976) (gray) and the model noise spectra for an rms error of about $9 \times 10^{-3}\,\mathrm{m\,s}^{-1}$ (dashed) are also shown. The shear noise spectrum is consistently corrected for the resolution and range smoothing of the ADCP. The GM spectra are computed using the local f, survey-average N, and 0.1 and 1 times the GM energy level for the frequency and wavenumber spectra, respectively.

b. WKB stretching

The varying vertical stratification is accounted for by using the Wentzel–Kramers–Brillouin (WKB) scaling (Leaman and Sanford 1975), using the survey-mean

stratification of $N_0 = 3.7 \times 10^{-3}\,\mathrm{s}^{-1} \equiv 2.12\,\mathrm{cph}$ as the reference buoyancy frequency. The stretched depth for a given $N(z)$ profile is

$$z_{\mathrm{wkb}} = \int_z^0 N(z)/N_0\, dz. \tag{1}$$

For reference, both the depth and stretched depth are shown in Fig. 6. Horizontal velocity and pressure scale as $[N_0/N(z)]^{1/2}$, and vertical displacement scales as $[N(z)/N_0]^{1/2}$. The stretched depth has nonuniform vertical resolution; therefore, the stretched profiles are interpolated to uniform 8-m vertical separation. Velocity scaling $(N_0/N)^{1/2}$ varies between 0.52 and 0.88. The stretched velocity profiles are normalized to preserve the total kinetic energy at each (original) profile.

c. *Horizontal kinetic energy, shear, strain, and Richardson number*

The profiles of horizontal kinetic energy (HKE) are computed from

$$\mathrm{HKE} = \frac{1}{2}\rho_0(u^2 + v^2), \tag{2}$$

after removing the depth average at each profile to approximate the baroclinic HKE. The profiles of shear squared are calculated as

$$\mathrm{Sh}^2 = (\partial u/\partial z)^2 + (\partial v/\partial z)^2. \tag{3}$$

ADCP shear is calculated over the 24-m vertical scale using 8-m resolution profiles. Profiles of HKE and Sh^2 derived from the ADCP and the XCPs are shown in Fig. 6, together with the buoyancy frequency profile, all calculated consistently at 24-m vertical scale using 8-m vertically averaged profiles. Because the XCPs are concentrated in the first half of the ADCP record, before day 116.5, time averaging of ADCP data in Fig. 6 is restricted to this period. This also corresponds to the period with elevated near-inertial signal presented in the next section. The Sh^2 and HKE derived from the two independent instruments compare well: averaged between 120 and 450 m, where data points are available from both instruments, HKE per unit mass measured by the ADCP and XCP is identical ($1.3 \times 10^{-4}\,\mathrm{J\,kg}^{-1}$). The Sh^2 derived using the ADCP is $4.4 \times 10^{-7}\,\mathrm{s}^{-2}$, approximately 25% larger than the XCP-derived value of $3.5 \times 10^{-7}\,\mathrm{s}^{-2}$.

The vertical resolution of the XCP profiles is better than 8 m, and the shear spectra are relatively noise free down to the 5-m vertical scale (not shown). In addition to the 24-m shear consistent with the ADCP calculations, higher-resolution shear is obtained as the slope of linear fits to 10-m segments of velocity against depth.

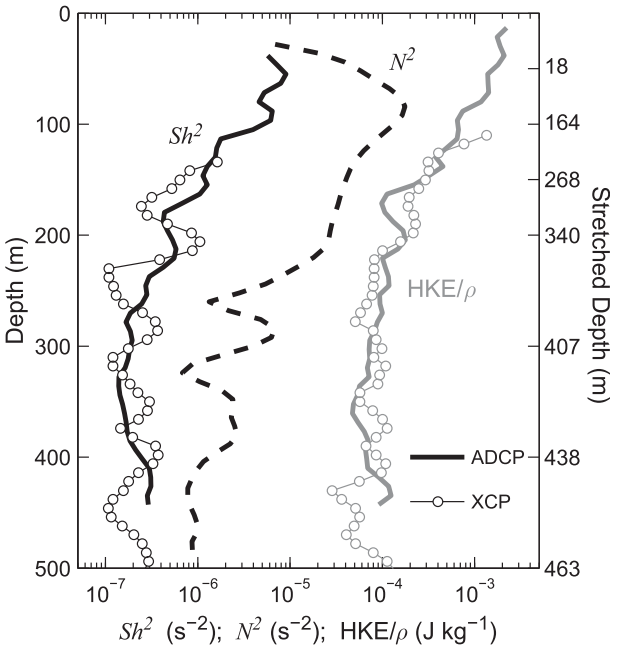

FIG. 6. Survey-averaged profiles of shear-squared Sh^2 from ADCP (thick black) and XCP (thin black, circles), buoyancy frequency N^2 (dashed), and horizontal kinetic energy per unit mass HKE/ρ_0 for ADCP (thick gray) and XCP (thin gray, circles). For reference, the stretched depth is shown on the right ordinate. Velocity profiles (both ADCP and XCP) are referenced to the mean between 200 and 450 m. All profiles are calculated consistently using 8-m vertical averages and 24-m vertical scale for gradients.

The 10-m shear is used to obtain a higher-resolution Richardson number, $\mathrm{Ri} = N^2/\mathrm{Sh}^2$. Accordingly, we have two estimates of Ri: one at 24-m vertical scale (ADCP) and a second one at 10-m vertical scale (XCP). To be consistent, the buoyancy frequency profile is calculated identically as the shear, using 8-m averages and 24-m gradients (for 24-m Ri) and using the vertical density gradient from the slope of linear fits to 10-m segments of density against depth (for 10-m Ri). In calculating the Richardson number, the segments of the profiles affected by the noise level of density and velocity gradient measurements are excluded whenever N is less than 1 cph or Sh^2 is less than $1 \times 10^{-6}\,\mathrm{s}^{-2}$ (section 4a). Resulting profiles of Ri are shown in Fig. 7. There are very few data points above the noise level below 300 m (for XCP) and below 160 m (ADCP). Overall, the ADCP-derived 24-m Ri is larger than the 10-m Ri from the XCPs; nevertheless, the profile suggests that the time-averaged low-resolution Ri approaches unity at the base of the mixed layer. Small values of Ri are more frequently observed in the 10-m Ri profiles and will be discussed in relation to mixing in section 5f.

Strain η_z is the vertical gradient of isopycnal displacements. In this study, η_z is computed from density profiles

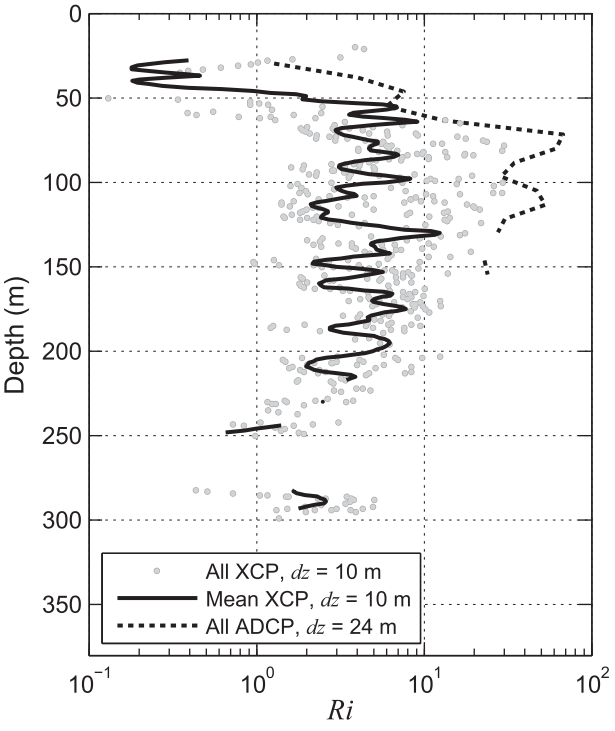

FIG. 7. Profiles of Richardson number calculated from the ADCP (dashed) using 24-m vertical scale and from the XCP measurements using 10-m vertical intervals. The XCP calculations are made by using corresponding $N(z)$ profiles and shear for each cast (markers) and using the survey-mean $N(z)$ profile and shear averaged over all XCP casts (solid line). The vertical scale used in $N(z)$ calculations is consistent with shear calculations. Values of N less than 1 cph and Sh^2 less than $1 \times 10^{-6}\,\mathrm{s}^{-2}$ are excluded.

measured by the microstructure profiler, relative to the time-mean density profile for each 15-h set of measurements. Isopycnals with 2-m mean vertical separations are used, and gradients are calculated over 24-m scale consistent with the Sh and N calculations.

d. 2D spectral estimates

Two-dimensional (2D), combined vertical wavenumber–frequency spectra $\Phi(m, \omega)$ are useful in separating cyclonic and anticyclonic rotary shears with positive and negative wavenumbers (see, e.g., Pinkel 2008). The four quadrants of a 2D spectrum with frequency on the x axis and wavenumber on the y axis can be interpreted as clockwise (CW; anticyclonic in the Northern Hemisphere) rotation in negative frequencies (left quadrants) and counterclockwise (CCW) rotation in positive frequencies (right quadrants). For freely propagating linear internal waves, downward-propagating energy (upward-propagating phase) corresponds to $\omega/m > 0$, whereas upward-propagating energy is in quadrants with $\omega/m < 0$. Typically, downward, near-inertial energy induced by wind forcing is expected in the lower-left quadrant ($\omega < 0$ and $m < 0$).

Wavenumber–frequency spectra are calculated as described in Pinkel (2008), see also Pinkel (1984), using the depth–time records of hourly averaged complex current, $U(z) = u + iv$. The velocity time series from 18 bins between the 45- and 190-m depths are WKB scaled and stretched (section 4b) prior to 2D Fourier transformation. The upper limit is chosen as the first bin below the mixed layer depth. The bottom limit is the deepest bin where the survey-averaged shear variance profile is above the noise level of $10^{-6}\,\mathrm{s}^{-2}$ (Fig. 6). The chosen depth range corresponds to a stretched depth of 11 to 325 m.

Two 48-h-long periods are analyzed; one relatively energetic period before day 116.5 and a second one after. The spectra are shown in Figs. 8 and 9, respectively (section 5a). Spectral estimates are corrected for the resolution and smoothing of the ADCP (section 4a). Horizontal kinetic energy spectral estimates are obtained by multiplying the velocity spectra by $0.5\rho_0$ to be used in calculations of energy fluxes in given ω and m bands. Shear spectra are obtained by weighting the velocity spectra by $(2\pi m)^2$. The noise dominates the shear spectra at $m > 0.04$ cpm. Because of the short length of the record, the frequency resolution is coarse: $0.374f$. Finally, one-dimensional spectra are obtained for each quadrant by integrating the 2D spectra in frequency and/or in wavenumber. The upper integration limit in wavenumber is set to 0.04 cpm to limit the influence of noise at high wavenumbers. The one-dimensional spectra inferred for each quadrant can be compared to the shear wavenumber spectrum presented in Fig. 5b. The latter includes contributions from all quadrants and is averaged over the entire duration of the experiment. The peak at order 100-m vertical scale, associated with the near-inertial negative frequencies discussed in section 5a, is not apparent in Fig. 5b.

5. Results and discussion

a. Spectral content

The average frequency spectrum of velocity and the vertical wavenumber spectrum of shear are shown in Fig. 5. There is a pronounced near-inertial peak that covers the inertial and the semidiurnal M_2 frequencies. The internal M_2 tides are evanescent at this latitude ($\omega_{M2} < f$) and cannot propagate freely. Also shown in Fig. 5 is the corresponding Garrett and Munk (GM) spectrum (Garrett and Munk 1975; Cairns and Williams 1976), calculated using the local f and survey-mean N. The GM frequency spectrum is one order of magnitude more energetic than the observations. The observed vertical wavenumber spectrum is comparable in

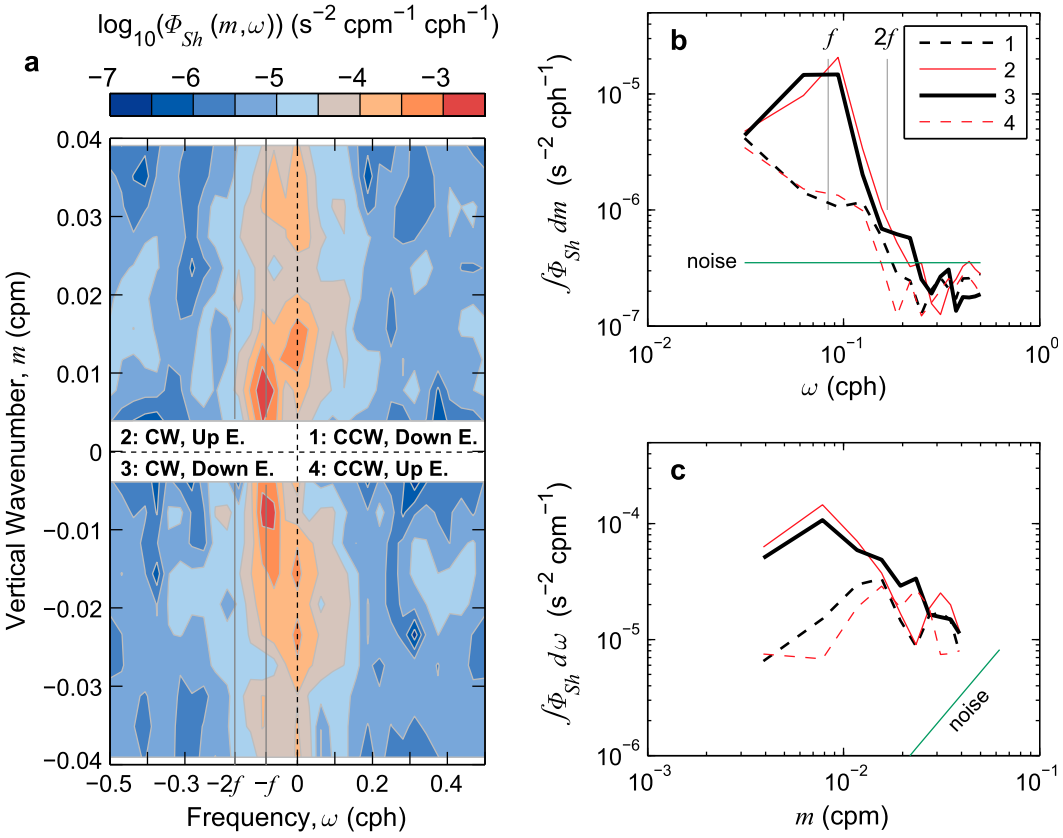

FIG. 8. Frequency (ω)–vertical wavenumber (m) spectra of shear derived from the ADCP measurements between 11 and 325 stretched m during Period 1 (day < 116.5). (a) Four-quadrant, two-dimensional spectra. Negative frequencies, quadrants 2 and 3, correspond to CW (anticyclonic) rotation, whereas the positive frequencies correspond to CCW rotation. Downward-propagating energy (upward-propagating phase) correspond to $\omega/m > 0$, that is, quadrants 1 and 3. Typically downward, near-inertial energy is expected in quadrant 3. One-dimensional (b) frequency and (c) wavenumber spectra are obtained by integrating the 2D spectra in wavenumber and in frequency, respectively. The green lines indicate the shear noise spectrum.

magnitude to GM; however, it differs in shape. When referenced to the GM model, the relatively elevated variance seen in the wavenumber spectrum compared to the frequency spectrum suggests excess energy in high vertical modes, which is an indication that the shear is primarily near inertial. The increase in the spectral level with increasing wavenumber at low wavenumbers is reminiscent of other wavenumber spectra from the Arctic environment (D'Asaro and Morehead 1991; Pinkel 2008; Fer et al. 2010). The frequency spectrum decays similar to the GM shape until approximately 2.5f and is affected by noise thereafter. When the model noise spectrum is removed, however, the resulting spectrum (thin black line in Fig. 5a) approximately follows the GM slope.

2D vertical wavenumber–frequency spectra $\Phi(m, \omega)$ for Period 1 (day < 116.5) and Period 2 (day > 116.5) are shown in Figs. 8 and 9, respectively, together with the one-dimensional spectra from each quadrant. Typically downward, near-inertial energy (anticyclonic, CW) induced by wind forcing is expected in the bottom-left quadrant ($\omega < 0$ and $m < 0$).

The frequency content for low frequencies, $\omega < 2f$, is more energetic in the anticyclonic quadrants relative to the quadrants with positive frequencies. This is true for both periods; however, during Period 1, the near-inertial band is approximately a factor of 4 more energetic than that in Period 2. The difference between the anticyclonic spectra, which are dominant near f, and the cyclonic spectra is significant at the 95% confidence level. For the anticyclonic spectra, the difference in the downward ($m < 0$) and upward ($m > 0$) energy is not significant at the 95% confidence level. The upward energy is typically not expected when the near-inertial wave energy is forced from the surface, such as by winds, and is discussed further in section 5h. The peak in quadrant 3 of Fig. 8a and the wavenumber content in the 1D spectra show that the near-inertial motions have a dominant vertical scale of 128 m. This near-inertial band shear

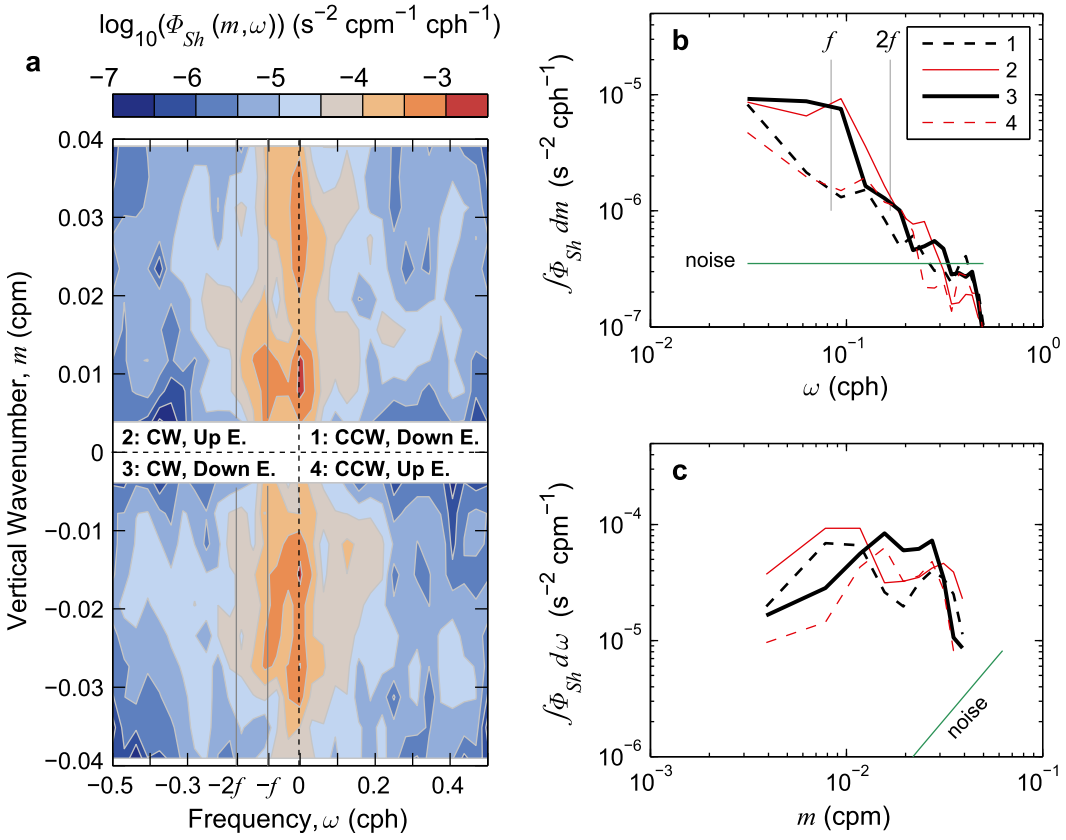

FIG. 9. As in Fig. 8, but for Period 2 (day > 116.5).

variance decays from Period 1 to Period 2, suggesting that the wave energy is dissipated or propagated away from the drifting ice floe.

While our dataset does not for allow the calculation of net energy fluxes because of large uncertainties (see section 5c), there is near-inertial energy of comparable magnitude in the upward- and downward-propagating components. This observation is possible only after partitioning the energy into wavenumber and frequency components through the 2D spectral analysis.

b. *Near-inertial band signal*

The observations show significant near-inertial variability. As an example, time series of zonal shear at the stretched depth $z_{\mathrm{wkb}} = 150$ m is shown in Fig. 10a. This level corresponds to approximately 90-m depth and is chosen because of its proximity to the depth of the stratification maximum and the subsurface dissipation maximum (Fig. 4). The shear at other depth levels in the upper 100 m is comparable, but at deeper levels it decays by one order of magnitude (Fig. 6). The near-inertial variability is the dominant feature in the time series shown in Fig. 10a.

To isolate the near-inertial band, a second-order Butterworth filter is applied with a passband bandwidth of 0.014 cph centered at the local inertial frequency of 0.0835 cph. Although a sharper filter is desirable, the edge frequencies are a compromise to limit the spurious oscillations near sharp transitions (ringing) of the filter.

The near-inertial variability visible in the nonfiltered data is isolated by the filter (Fig. 10a). The attenuation of the amplitude is not an artifact of the filter. The properties of the filter, in particular the ringing effect, are demonstrated by filtering a pulse of $u_z = -1 \times 10^{-3}\,\mathrm{s}^{-1}$, using the same filter. In Fig. 10b, the filtered pulse signal is multiplied by 50 to illustrate that the filter effects do not degrade the data. The ringing in response to the pulse is clearly visible, but with an amplitude of at least 50 times less than the observed magnitude that vanishes relatively quickly (the ratio of the filtered amplitude at peak 1 to peak 4 is 1.4 for u_z and about 15 for the filtered pulse signal).

Time–depth distributions of the near-inertial bandpassed strain and shear are shown in Fig. 11 for the upper 210 m. The plotting range (340-m stretched depth) is chosen to bring out the shear and strain signals above the deeper levels where the shear is noisy and the strain is dominated by nonwave signals. The distributions are dominated by bands of alternating positive and negative

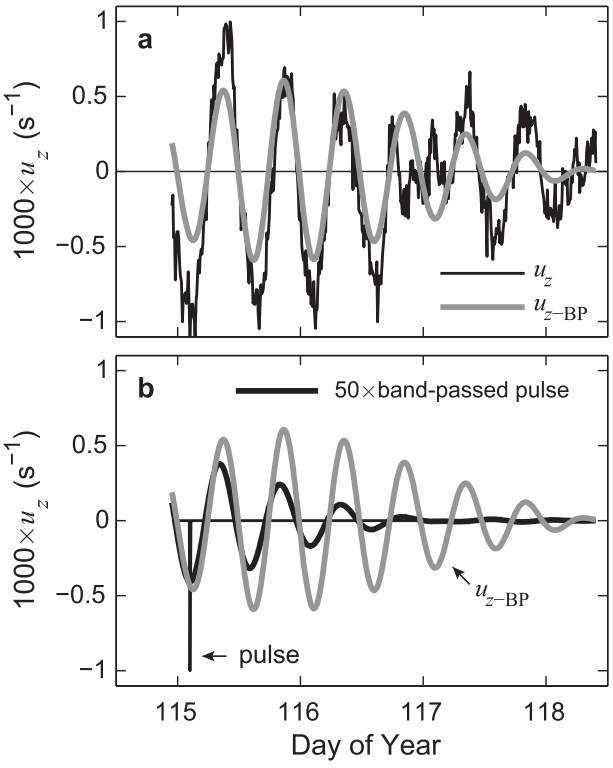

FIG. 10. Time series of (a) the zonal component of shear u_z measured at 150-m stretched depth together with its bandpassed record (u_{z-BP}, gray) and (b) a pulse of -10^{-3} s^{-1} (thin black) introduced at the same time as the first observed u_z minimum and its response after filtering, multiplied by a factor of 50 for clarity. The filtered shear signal of (a) is redrawn for reference.

values with slanted phase lines. A combination of both upward and downward propagation of phase is visible. Bandpassed shear and strain time series extracted at $z_{wkb} = 150$ m show how the amplitude of the variability vanishes in time (Fig. 11e). The phase, $\phi = \arctan(v_z/u_z)$, inferred from the zonal and meridional components of the shear agrees with a slightly superinertial periodicity of $1.03f$ and rotates clockwise in time ($\partial\phi/\partial t > 0$), consistent with a near-inertial wave (Fig. 11e).

The near-inertial wave with frequency $1.03f$ and vertical scale of 128 m can be compared to the observations from lower latitudes. In the Sargasso Sea, D'Asaro and Perkins (1984) observed a net downward propagation of energy, associated with near-inertial waves with peak frequency of about $1.06f$. Near Mendocino Escarpment in the eastern Pacific Ocean (approximately 40°N), a site where internal tides would be expected to dominate, Alford (2010) observed energetic near-inertial waves in the entire water column (3700-m water depth), radiating both upward and downward. The wave packets were associated with frequencies of $(1.04–1.06)f$ and vertical scales of 130–350 m. Observations in the upper 200 m of the Banda Sea revealed an energetic near-inertial wave packet with observed frequency $1.02f$ and vertical scale 100 m (Alford and Gregg 2001).

c. *Energy and energy flux*

Vertical group velocity and upward and downward energy fluxes are calculated for selected wavenumber m and frequency ω bands using the 2D energy spectra. The dispersion relation for near-inertial waves (i.e., $\omega \ll N$) with horizontal wavenumber k_H is

$$k_H^2 N^2 = m^2(\omega^2 - f^2). \tag{4}$$

The vertical group velocity C_{gz} is inferred from the dispersion relation as

$$C_{gz} = \frac{\omega^2 - f^2}{\omega m}. \tag{5}$$

The energy flux is

$$F_{u,d} = \int_m \int_\omega E_{u,d}(\omega, m) C_{gz}(\omega, m), \tag{6}$$

where the subscripts u and d indicate the upward- and downward-propagating components, and E is the horizontal kinetic energy spectral estimate outlined in section 4d. Because for near-inertial waves the kinetic energy is much larger than the potential energy, we assume that the total energy can be approximated by the kinetic energy alone. Total wave kinetic energy is then $E_t = E_d + E_u$, and the net energy flux is $F_u - F_d$. Because of the large uncertainty (see below), we cannot distinguish the net energy flux and exclude it from the discussion.

The energy flux estimates suffer from large errors in the group velocity, primarily because of the low-frequency resolution. Relative error in the group velocity is estimated using the propagation of errors formula, assuming the errors associated with the frequency and wavenumber are uncorrelated (Emery and Thomson 2004):

$$\frac{\delta C_{gz}}{C_{gz}} = \left[\left(\frac{\partial C_{gz}}{\partial \omega} \delta\omega \right)^2 + \left(\frac{\partial C_{gz}}{\partial m} \delta m \right)^2 \right]^{1/2}. \tag{7}$$

Here the errors in ω and m follow from the Rayleigh's criterion $\delta\omega = 1/120$ cph and $\delta m = 1/256$ cpm. The error for the energy is calculated similarly using an error velocity of 1 cm s^{-1}.

Results for the near-inertial frequency bands in the low wavenumbers are tabulated in Table 1 for Periods 1 and 2, separately. The energy is integrated in the wavenumber band 1/256 to 1/128 cpm for the first three

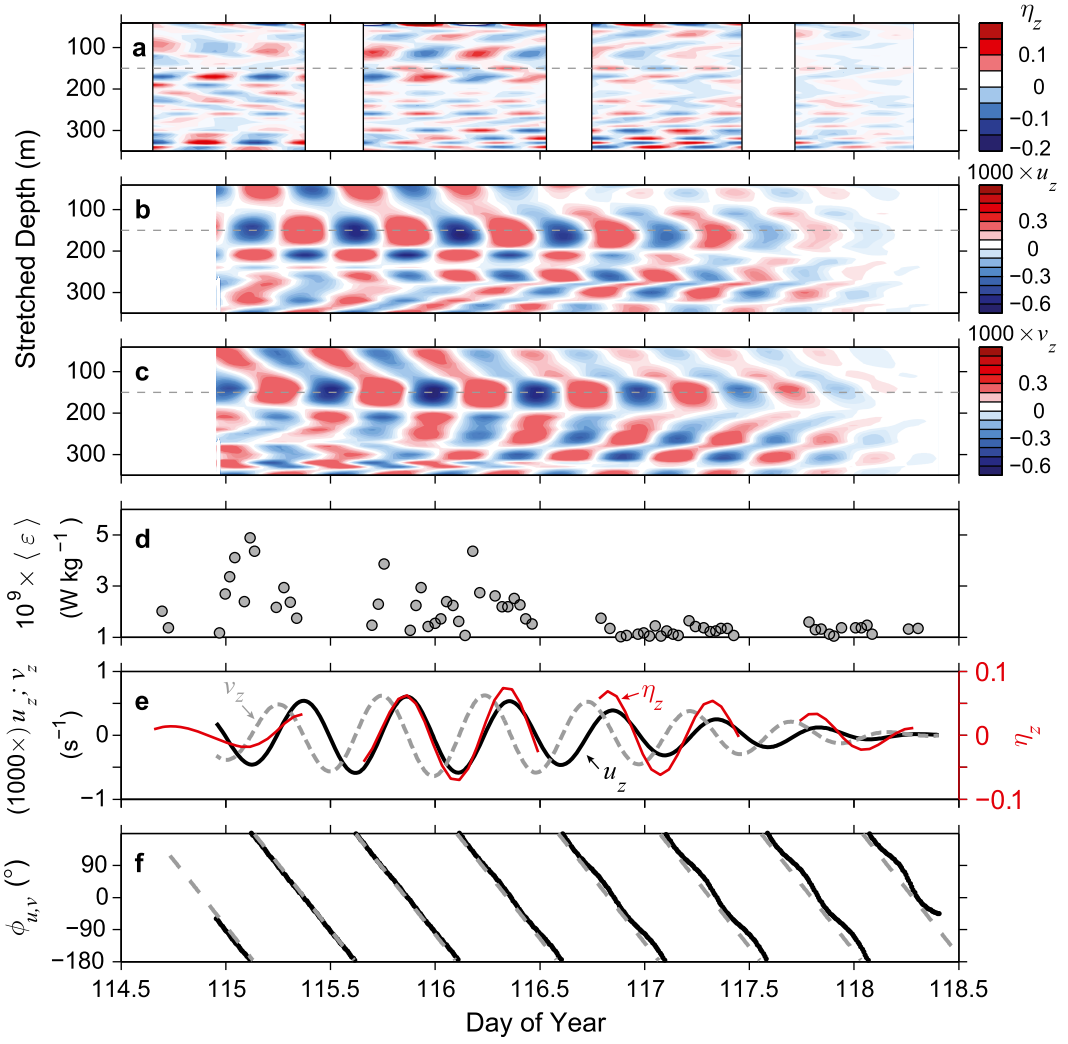

FIG. 11. Time series of near-inertial bandpassed (a) strain η_z, (b) zonal shear u_z, and (c) meridional shear v_z, plotted vs WKB-stretched depth, corresponding to 50- to 210-m meters range below the ice. Time series of (d) dissipation rate averaged in the pycnocline between 70- and 150-m $\langle \varepsilon \rangle$, (e) u_z (black), v_z (gray), and η_z (red) extracted at $z_{\mathrm{wkb}} = 150$ m [dashed lines in (a)–(c)], and f) (black) the corresponding phase $\phi = \arctan(v_z/u_z)$ together with near-inertial periodicity of 1.03f (gray dashed).

near-inertial frequency bands centered at $\omega/f = 1.122$, 1.496, and 1.87. Note that the frequency resolution is 0.374f, and the first frequency band spans 0.935 to 1.309f, including the observed 1.03f (Fig. 11f). For the 128–256-m vertical scale, integrated over the low near-inertial frequencies, there is vertical symmetry in the energy flux during both periods (i.e., $F_u \sim F_d$ within the errors).

Total energy, downward energy, and the energy fluxes are summarized in Table 2, integrated over the three near-inertial frequency bands. Integration in wavenumber is done over the low-wavenumber band as well as over the wavenumbers up to 1/51 cpm. Inclusion of the high wavenumbers increases the energy by only 20% in Period 1 and 40% in Period 2, insignificant when the error bars are taken into account. In the low-wavenumber band, Period 1 is 3 times more energetic than Period 2.

The energetics can be compared to the observations of Halle and Pinkel (2003) from the Beaufort Sea during the winter of 1993/94. Upward-propagating near-inertial wave packets were equally common as downward-propagating ones. Their calculations over f–2f and 15–140-m scales show symmetric upward and downward fluxes of about (3–4) $\times$ 10^{-5} W m^{-2} in the deep Canada basin and (4–6) $\times$ 10^{-5} W m^{-2} over the Northwind Ridge. The fluxes in the f–2f band observed from Barneo (reported in the last row of Table 1) are one to two orders of magnitude larger (partly because of including larger vertical scales to 256 m and partly

TABLE 1. Upward F_u and downward F_d near-inertial energy flux ($10^5\,\mathrm{W\,m^{-2}}$) for the wavenumber bands 1/256 and 1/128 cpm, inferred for Periods 1 and 2. The frequency ω is normalized by the local inertial frequency f. The vertical group velocity C_{gz} ($10^3\,\mathrm{m\,s^{-1}}$) is given as the range obtained for each wavenumber band. The energy fluxes are computed using the group velocity averaged over the two wavenumber bands. The uncertainty of C_{gz} is given in percent, obtained using Eq. (7). The uncertainty in the energy flux is estimated from the error in C_{gz}.

		F_u	F_d	F_u	F_d
		Period 1: day < 116.5		Period 2: day > 116.5	
ω/f	C_{gz}				
1.122	0.7–1.4 (92%)	78 ± 72	51 ± 47	26 ± 24	12 ± 11
1.496	2.5–4.9 (53%)	49 ± 26	19 ± 10	25 ± 13	3 ± 2
1.870	4.0–7.9 (51%)	9 ± 5	3 ± 2	12 ± 6	8 ± 4
Total	—	136 ± 77	73 ± 48	63 ± 28	23 ± 12

because of a more energetic wave field). Recalculating the fluxes between 51- and 128-m scales reduces the total fluxes to (15–60) $\times\ 10^{-5}\,\mathrm{W\,m^{-2}}$, 5 to 10 times larger than the observations from the Beaufort Sea.

d. Wind work

When the surface is ice covered, the wind stress–related turbulence production is due to the rate of work done by stress under the ice. Ice encounters drag from the water below as the floe moves in response to wind. The induced momentum flux at the ice–ocean interface can be described using a friction velocity u_{*0}. Work done by stress under the ice can be calculated as $F_W = \rho_0 u_{*0}^3$. The friction velocity is obtained using the Rossby similarity method described in McPhee et al. (2003). This is analogous to relating wind stress at the surface to the geostrophic wind. An underice roughness length of 0.01 m, representative of multiyear ice from NPEO drift stations, is used (McPhee et al. 2003). The mean ice velocity is 0.10 and $0.07\,\mathrm{m\,s^{-1}}$ during Periods 1 and 2, respectively. When averaged over the entire drift, the wind work is $17 \times 10^{-5}\,\mathrm{W\,m^{-2}}$ and is not significantly different when averaged over each period separately (Table 3). Note that the analysis Period 1 does not cover the windy period early in the drift (see Fig. 3a), nor the storm period prior to the experiment; hence, the actual wind work resulting in the near-inertial response during our observations is not known. A rough estimate of a range of energy flux input F_W representative of the storm period can be made by assuming a mean wind speed bounded by 10 and $15\,\mathrm{m\,s^{-1}}$. Ice velocity scales roughly as 2% of the wind speed (see Fig. 3a), giving F_W in the range of 150 to $440 \times 10^{-5}\,\mathrm{W\,m^{-2}}$.

The main source of error in u_{*0} is the underice roughness length, which can range from hydraulically smooth (5×10^{-5} m) under fast ice to several centimeters in the marginal ice zone. A representative value range is 5×10^{-3} to 3×10^{-2} m (McPhee et al. 2003). Reducing or increasing the roughness length used in the calculation by a factor of 2 leads to a 25% reduction or 30% increase in F_W and its standard deviation.

TABLE 2. Total E_t and downward E_d near-inertial energy and total dissipation under ice D_M, following Morison et al. (1985). Range indicates the wavenumber band used in calculations. Uncertainty in energy is estimated by propagating an error velocity of $10^{-2}\,\mathrm{m\,s^{-1}}$. Uncertainty in D_M is due to the error in the total energy.

		Range (cpm)	Period 1	Period 2
E_t	$\mathrm{J\,m^{-3}}$	1/256–1/128	1.5 ± 0.6	0.5 ± 0.3
		1/256–1/51	1.8 ± 0.6	0.7 ± 0.4
E_d	$\mathrm{J\,m^{-3}}$	1/256–1/128	0.6 ± 0.4	0.1 ± 0.1
		1/256–1/51	0.7 ± 0.4	0.2 ± 0.2
F_d	$\times 10^5\,\mathrm{W\,m^{-2}}$	1/256–1/128	73 ± 48	23 ± 12
		1/256–1/51	81 ± 53	32 ± 17
F_u	$\times 10^5\,\mathrm{W\,m^{-2}}$	1/256–1/128	136 ± 77	63 ± 28
		1/256–1/51	147 ± 83	86 ± 38
D_M	$\times 10^5\,\mathrm{W\,m^{-2}}$	1/256–1/128	102 ± 41	24 ± 14
		1/256–1/51	122 ± 41	33 ± 19

e. Dissipation under ice

Internal waves are expected to dissipate a fraction of their energy when they contact the ice. According to Morison et al. (1985), the total dissipation, in units of $\mathrm{W\,m^{-2}}$, in the oscillatory underice boundary layer from a wave field with total energy E_t ($\mathrm{J\,m^{-3}}$) is

$$D_M = 2CV_{\mathrm{ice}}E_t, \tag{8}$$

where $C = 3.4 \times 10^{-3}$, and V_{ice} is the velocity of the ice floe. Calculated values of D_M are listed in Table 2. The total dissipation under ice, in each period, is comparable to F_u or F_d. The term D_M can be compared to the depth-integrated dissipation rate D_I, obtained from the microstructure observations,

TABLE 3. Wind work under ice F_W averaged over each period (± one standard deviation), total dissipation under ice D_M (± uncertainty) in the wavenumber band 1/256 to 1/51 cpm, and depth-integrated dissipation D_I from microstructure measurements. The depth range of integration for D_I is indicated. A rough estimate of F_W representative of the storm period prior to the experiments is in the range of 150 to $440 \times 10^{-5}\,\mathrm{W\,m^{-2}}$ (section 5d). Units for all quantities are $10^5\,\mathrm{W\,m^{-2}}$.

	Period 1	Period 2
F_W	17 ± 13	15 ± 8
D_M	122 ± 41	33 ± 19
D_I, 0–8 m	130	10
D_I, 0–38 m	230	22
D_I, 0–190 m	250	39

$$D_I = -\rho_0 \int_z^0 \varepsilon(z)\, dz, \tag{9}$$

by integrating the dissipation profile averaged in Periods 1 and 2. In practice, the uppermost available good data point for the dissipation rate, which is about 3 m below the ice, is extended upward to $z = 0$. Integration is made over an 8-m-thick underice boundary layer. The boundary layer thickness is taken as the minimum observed outer layer thickness $0.4u_{*0}/f$ (McPhee 2008), which varied between 8 and 18 m. Resulting values of D_I are given in Table 3, which also includes integrations to deeper levels for a later discussion.

Depth-integrated dissipation rates D_I are comparable with D_M. It should be noted that D_I comprises dissipation from all resolved time and space scales, whereas D_M is calculated for the near-inertial frequency band and up to 1/51 cpm. During both periods, D_I in the upper 8 m is equal to D_M within the error bars. With the caveat of large measurement uncertainties, our observations imply that total dissipation under ice is substantial on the order of 100 and $10 \times 10^{-5}\,\mathrm{W\,m^{-2}}$ in Periods 1 and 2, respectively. In the following, we will therefore assume that upward energy is dissipated immediately below the ice (within 8 m).

f. Role in mixing

We hypothesize that the relatively elevated level of dissipation rate below the mixed layer depth, centered at the pycnocline (see Fig. 4c), is due to near-inertial waves. The dissipation rates averaged in the pycnocline (between 70- and 150-m depth) $\langle\varepsilon\rangle$ are up to a factor of 5 larger in the first half of the record when the near-inertial signal is strong (Fig. 11d). When averaged in time before day 116.5 (Period 1), $\langle\varepsilon\rangle$ is $2.3 \times 10^{-9}\,\mathrm{W\,kg^{-1}}$, approximately a factor of 2 larger than the time average in the remaining period.

We observe significant coherency in the near-inertial frequency band between the dissipation rate averaged in the pycnocline $\langle\varepsilon\rangle$ and shear and strain (Fig. 12). Coherency spectra are calculated from the time series at 11 levels, separated by 8 m between 70 and 150 m. The coherency is largest between $\langle\varepsilon\rangle$ and the zonal shear with the latter leading by approximately 35°. Near-inertial strain is approximately in phase with $\langle\varepsilon\rangle$. In the Banda Sea, Alford and Gregg (2001) observed dissipation and eddy diffusivity coherent with a shallow downward-propagating near-inertial wave. While near-inertial shear was important to reduce the Ri, the strain was important in modulating Ri once per wave cycle. A similar process was observed in the Mendocino Escarpment (Alford 2010). Although shear was weaker there, so was the stratification; hence, the shear and strain modulation led to sufficiently low Ri and mixing events. The profiles of Ri from Barneo drift presented in Fig. 7 suggest that the near-inertial shear and strain can act to reduce Ri, particularly at the base of the mixed layer, and contribute to turbulence generation. Higher-resolution profiles inferred from the XCPs suggest that values of Ri near unity are plausible deeper in the water column between 100 and 250 m, which can explain the slightly elevated dissipation rates in the water column (Fig. 4c).

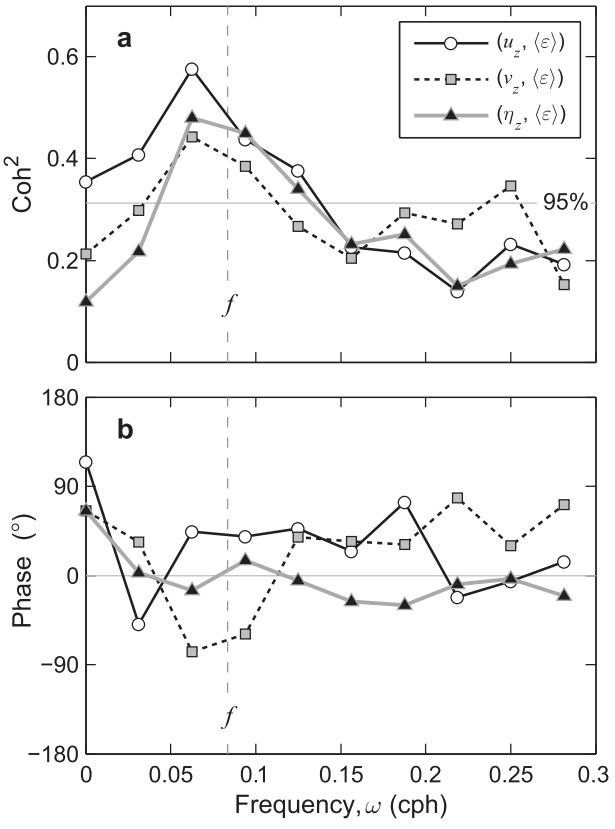

FIG. 12. (a) Coherency squared and (b) phase between pycnocline-averaged dissipation rate $\langle\varepsilon\rangle$ and zonal shear u_z (circles), meridional shear v_z (squares), and strain η_z (triangles). Spectra are computed over 11 levels, separated by 8 m between 70 and 150 m. The FFT length is 32, giving three spectra at each level (6 degrees of freedom), and we assume that every third level is independent, giving an effective degrees of freedom of 18. Only the coherency values above the horizontal gray line are significantly different than zero at the 95% confidence level. The inertial frequency f is indicated by vertical dashed lines.

The measurements from the Barneo drift suggest near-inertial modulation of Ri and the dissipation rate in the pycnocline. The time series of shear, strain, and dissipation rate, each averaged in the pycnocline between 70- and 150-m depth, are shown in Fig. 13 together with the Ri. The ADCP data are hourly values (not bandpass filtered), whereas strain and dissipation rate are shown

for each microstructure profile. When averaged between 70- and 150-m depth, the Richardson number is large (dashed line in Fig. 13d) because averaging smooths out the vertical gradients. When calculated at a single level (using $dz = 24$ m), the near-inertial modulation of Ri becomes apparent. Centered at 100-m depth, just below the depth of N maximum (Fig. 4b), Ri derived from the ADCP data is reduced to relatively small values. Values derived from the available XCP profiles at 10-m vertical scale (again centered at 100-m depth) are smaller, implying that Ri can attain values favoring turbulence production at smaller vertical scales.

Depth-integrated dissipation rate is computed [Eq. (9)] over the mixed layer depth (38 m) and down to 190 m, covering the depth range used for the spectral wave energy calculations. Resulting values of D_I are given in Table 3. For reference, if the entire upper 190 m were at a noise level of 10^{-10} W kg^{-1}, D_I would have been about 20×10^{-5} W m^{-2}. Period 1 with substantial near-inertial energy is also associated with significantly larger dissipation rates in the water column, compared to Period 2. Near-inertial waves appear to contribute significantly to the turbulence levels in the upper 150 m that compose the CHL, a crucial player in the Arctic Ocean stratification.

In the mixed layer, after removing the contribution in the upper 8 m, there is still about 100×10^{-5} W m^{-2} dissipation in Period 1 and another 20×10^{-5} W m^{-2} below the mixed layer. The wind work done beneath the ice, in the mixed layer, can be interpreted as the near-inertial energy flux at the surface. Ignoring lateral fluxes, the difference between the observed downward flux and the wind work would imply dissipation over the depth range below the mixed layer depth and down to 190 m (i.e., depth range of energy flux calculation). During Period 1, the near-inertial F_d is about 73 ($\pm$48) $\times$ 10^{-5} W m^{-2}. A rough estimate of the wind work F_W, representative of the storm period, is in the range of 150 to 440 $\times$ 10^{-5} W m^{-2} (section 5d). The difference $F_W - F_d$ could account for the depth-integrated dissipation below 8 m in Period 1. During Period 2, $F_W - F_d$ in the near-inertial band is not significantly different than zero, consistent with D_I below the mixed layer near noise level. Overall, our measurements indicate that a significant fraction of the dissipation observed in the upper 200 m can be explained by the energy flux in the near-inertial wave field.

Despite the bulk agreement between the energetics and the measured dissipation rates, the decay of the near-inertial signal in time (Fig. 11) appears to be extremely rapid for near-inertial waves. Mixing associated with near-inertial internal waves has been previously observed elsewhere (see, e.g., Gregg et al. 1986; Alford and Gregg 2001). In the Banda Sea, Alford and Gregg (2001) estimated the length of time the inertial wave would survive to be between 10 and 100 days. The wave lost little energy as it propagated to the stratification maximum, but lost most of its energy in a mixing region below. The near-inertial feature and the mixing patch reported in Gregg et al. (1986) faded out after 3 days (a time scale comparable to our observation). It was not possible, however, to determine whether the decay was due to turbulent mixing or the instrument drifting away from the wave. Assuming that the energy is extracted from the downward near-inertial internal waves at a slow rate, a time scale for dissipation of the internal wave field is (Gregg et al. 1986)

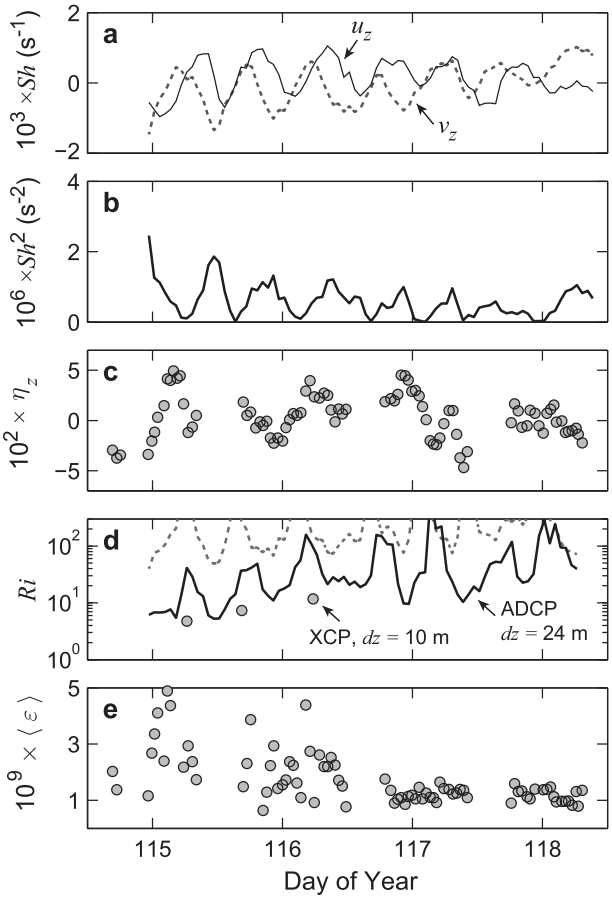

FIG. 13. Time series of (a) zonal shear u_z (solid) and meridional shear v_z (dashed), (b) shear squared Sh^2, (c) strain η_z, (d) Richardson number Ri, and (e) pycnocline-averaged dissipation rate $\langle \varepsilon \rangle$. Shear and strain are averaged in the pycnocline, between 70 and 150 m, consistent with $\langle \varepsilon \rangle$. The Ri is shown for (dashed) pycnocline-averaged shear and stratification as well as the time series centered at 100-m depth (solid), both calculated using 24-m vertical resolution and 8-m vertical averages. The bullets in (d) show Ri centered at 100-m depth, calculated from 10-m vertical resolution using the XCP profiles.

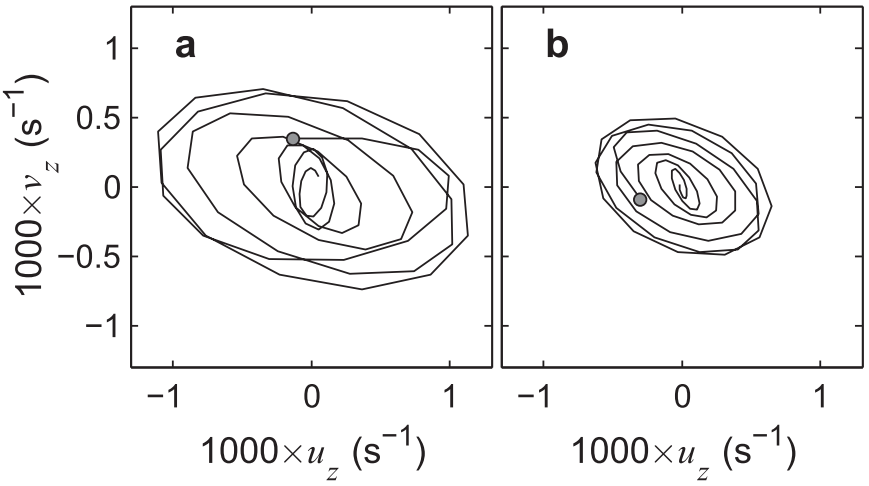

FIG. 14. Hodographs from the near-inertial bandpassed shear vectors at (a) 63- and (b) 80-m depths. Shear components are obtained from the ADCP using 24-m vertical scale. The circle marks the start of the hourly time series. The principal axes of the ellipses are oriented at 107° and 118° from the north, respectively.

$$T_d = E_d/\rho_0\varepsilon. \tag{10}$$

Here the dissipation rate of turbulent potential energy, which typically accounts for only 15% of the total dissipation, is excluded from the denominator. Using the downward energy of about $0.7\,\mathrm{J\,m^{-3}}$ during Period 1 (Table 2) and the average value of ε below the mixed layer of $1.3 \times 10^{-9}\,\mathrm{W\,kg^{-1}}$, the dissipation time scale is obtained as 6 days. This is approximately twice the time scale of the decay seen in Fig. 11. The lateral scales of the wave and the drift distance are comparable, and they propagate in opposite directions (section 5g). We therefore cannot confidently determine whether the decay of the wave energy is due to turbulent mixing or because we drifted away from the wave packet; probably a combination of the two. Nevertheless, the near-inertial band energy, largely neglected in the Arctic Ocean, can be an important source of turbulence in the upper ocean covering the cold halocline layer.

g. *Horizontal propagation direction*

The phase between shear and strain can be used to determine the horizontal propagation direction of the wave (see, e.g., Alford and Gregg 2001). Determination of the propagation direction is uncertain because of the low-frequency resolution and gaps in the strain time series (Fig. 11a). Using the coherency spectrum between zonal shear and strain, the relative phase is obtained in the near-inertial frequency band (Fig. 12). Averaging over only the coherency values significantly greater than nil (at 95% confidence level), the relative phase between the zonal shear and strain indicates a southeast propagation direction of 128° from the north. An alternative estimate can be made from the shear vector hodographs (Fig. 14). If most of the variance in shear is due to near-inertial waves, shear ellipses are expected to align with the wave propagation direction (Alford and Gregg 2001). The direction inferred from the phase difference between u_z and η_z is consistent with the orientation of the shear hodographs with the principal axis of about 110° and 120°.

If we bound the frequency of the wave with $1.01f$ and $1.1f$, using N_0, $m = 1/128$ cpm, and the dispersion relation [Eq. (4)], the horizontal wavelength is 7 to 23 km. The wave packet that fills a 200-m stretched depth (Fig. 11) thus extends about 10–35 km laterally. During the analysis period when the ADCP was operating ($114.5 <$ day < 118.5), the total lateral drift of the camp was about 26 km (Fig. 1). From the start of the GPS record to day 116 when there is a turn in the drift direction, the drift is 30 km, directed at 234° from the north, that is, toward the southwest. The wave thus propagates away from the drifting ice floe at a relative angle of 100°–130°. The lateral scales of the wave and the drift distance are comparable. While we discuss the possibility that the decay of the near-inertial shear is due to turbulence dissipation and mixing (section 5f), part of the decay can simply be because we are drifting away from the wave packet.

h. *Speculation on upward energy*

The presence of upward energy is counterintuitive when the near-inertial wave energy is forced from the surface. At this latitude, we cannot differentiate between the near-inertial waves and internal M_2 tides with our short time series. Internal tides can be generated

over topography (such as ridges) with energy propagating along beams emanating from the generation site, hence typically leading to upward energy propagation. The tides are weak in the central Arctic Ocean and the semidiurnal waves are evanescent. The drift is several hundreds of kilometers away from the nearest topographic feature, the Lomonosov Ridge (Fig. 1). We therefore cannot attribute the upward energy to internal tides in our dataset. An alternative is that we observe bottom reflections, propagating upward, of previously generated downward, near-inertial waves (Pinkel 2005). However, in the Arctic the typical near-inertial waves are expected to survive only a single bounce (Pinkel 2005) because of the dissipation under ice. The microstructure measurements reported here show substantial total dissipation in the under ice boundary layer and in the upper mixed layer (section 5e).

Groups of upward-propagating waves in the Arctic Ocean have been observed before (e.g., Merrifield and Pinkel 1996; Halle and Pinkel 2003). Detailed calculations by Halle and Pinkel (2003) show nearly equal up- and downward near-inertial energy fluxes in the deep Canada basin and over the Northwind Ridge (see their Table 3). Pinkel (2005)'s observations during SHEBA drift are rich in upward-propagating near-inertial energy. Merrifield and Pinkel (1996) suggested that a storm is a localized quasigeostrophic impulse, and the upward inertial waves are a part of the quasigeostrophic adjustment to this impulse. In our dataset, near-inertial wave–mesoscale interactions are possibly responsible for the upward energy. Such interactions are expected when the background vorticity modifies the effective inertial frequency and/or the background shear is sufficiently strong to block and upward reflect downward waves. According to the near-inertial chimney concept of Lee and Niiler (1998), downward-propagating near-inertial waves in positive background vorticity (e.g., outer regions of an eddy) suffer a reduction in speed and can be reflected (Halle and Pinkel 2003). The vertical component of the relative vorticity,

$$\zeta_z = \frac{\partial v}{\partial x} - \frac{\partial u}{\partial y}, \tag{11}$$

cannot be computed with our dataset. An estimate of ζ_z is made assuming a frozen mesoscale field. The so-called poor man's vorticity (PMV) is calculated following Halle and Pinkel (2003) as described in their appendix D:

$$\mathrm{PMV} = 2\frac{\partial v_\perp}{\partial c}, \tag{12}$$

where $v_\perp$ is the component of the subinertial current perpendicular to the drift direction, and c is the along-drift coordinate. PMV is an approximation to ζ_z and is equal to it in a region of uniform relative vorticity. In practice, PMV is calculated using the component of the subinertial absolute velocity normal to the drift direction of the ice camp relative to the motion of the current. Velocity of the ice relative to water and the absolute velocity are 15-h low-pass filtered using a fourth-order Butterworth filter. PMV is negative for clockwise rotation viewed from above. Early in the drift, PMV is positive (Fig. 15) with an amplitude exceeding 0.3*f*, suggesting significant near-inertial wave–mesoscale interaction and possibly reflection. The positive vorticity is likely the ridge of an anticyclonic (negative vorticity) eddy that was generated during the storm. Halle and Pinkel (2003) show examples of negative vorticity core eddies surrounded by positive vorticity ridges, typical in the Arctic Ocean.

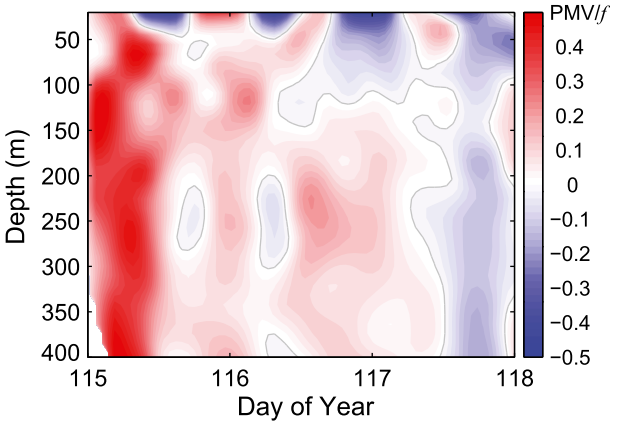

FIG. 15. Contours of the vertical component of relative vorticity (PMV) normalized by the local Coriolis parameter *f*. The PMV is smoothed over approximately 20 m in depth and 6 h in time. Positive values indicate cyclonic rotation when viewed from above.

6. Concluding remarks

Observations of horizontal currents, hydrography, and shear microstructure are reported from the central Arctic Ocean, collected from a drift about 10 days after a storm event and severe ice deformation period. Near-inertial frequency band motions appear in shear and strain. The near-inertial oscillations are most pronounced early in the measurement period, with comparable upward- and downward-propagating energy. The direction of net energy propagation cannot be distinguished due to the large error bars.

Rough estimates of wind work and the near-inertial energy flux imply that the waves were likely generated by the previous storm. Both the amplitude of the oscillations and the pycnocline-averaged dissipation rate gradually decay with time. The time scale of the

observed decay is approximately twice the rate implied by the reduction of energy over time. We cannot determine confidently whether the wave energy fade out is because of turbulent mixing or because the wave packet propagated away from the measurement site.

Dissipation rate of turbulent kinetic energy averaged in the pycnocline is near-inertially modulated. In the near-inertial frequency band, the coherency is large between the dissipation rate and shear and strain. Time series of the Richardson number suggest that the near-inertial shear and strain contribute to turbulence generation at the pycnocline. Depth-integrated dissipation measurements from the microstructure profiler show substantial total dissipation in the upper water column, below the mixed layer, covering the cold halocline layer. A rough estimate of the difference between the wind work done during the previous storm and the near-inertial energy flux below the pycnocline at the time of measurements is found to be comparable to the total dissipation beneath the upper mixed layer. Dissipation of near-inertial wave energy in the upper ocean is of crucial importance in the Arctic Ocean and must be properly accounted for. If sufficiently elevated, the dissipation can play a significant role in irreversible vertical mixing in the Arctic Ocean, in the cold halocline layer in particular.

Acknowledgments. This study is funded by the Research Council of Norway through the NORKLIMA Young Investigator Grant for IF (178641/S30). Comments from two anonymous reviewers were very helpful in improving an earlier version of the manuscript.

REFERENCES

Alford, M. H., 2010: Sustained, full-water-column observations of internal waves and mixing near Mendocino Escarpment. *J. Phys. Oceanogr.,* **40,** 2643–2660, doi:10.1175/2010JPO4502.1.

——, and M. C. Gregg, 2001: Near-inertial mixing: Modulation of shear, strain and microstructure at low latitude. *J. Geophys. Res.,* **106,** 16 947–16 968, doi:10.1029/2000JC000370.

——, M. F. Cronin, and J. M. Klymak, 2012: Annual cycle and depth penetration of wind-generated near-inertial internal waves at Ocean Station Papa in the northeast Pacific. *J. Phys. Oceanogr.,* **42,** 889–909, doi:10.1175/JPO-D-11-092.1.

Cairns, J. L., and G. O. Williams, 1976: Internal wave observations from a midwater float, 2. *J. Geophys. Res.,* **81,** 1943–1950, doi:10.1029/JC081i012p01943.

Comiso, J. C., 2012: Large decadal decline of the Arctic multiyear ice cover. *J. Climate,* **25,** 1176–1193, doi:10.1175/JCLI-D-11-00113.1.

D'Asaro, E. A., and H. Perkins, 1984: A near-inertial internal wave spectrum for the Sargasso Sea in late summer. *J. Phys. Oceanogr.,* **14,** 489–505, doi:10.1175/1520-0485(1984)014<0489:ANIIWS>2.0.CO;2.

——, and M. D. Morehead, 1991: Internal waves and velocity fine structure in the Arctic Ocean. *J. Geophys. Res.,* **96,** 12 725–12 738, doi:10.1029/91JC01071.

——, and J. H. Morison, 1992: Internal waves and mixing in the Arctic Ocean. *Deep-Sea Res.,* **39,** S459–S484, doi:10.1016/S0198-0149(06)80016-6.

——, C. C. Eriksen, M. D. Levine, P. Niiler, C. A. Paulson, and P. Vanmeurs, 1995: Upper-ocean inertial currents forced by a strong storm. Part I: Data and comparisons with linear theory. *J. Phys. Oceanogr.,* **25,** 2909–2936, doi:10.1175/1520-0485(1995)025<2909:UOICFB>2.0.CO;2.

Emery, W. J., and R. E. Thomson, 2004: *Data Analysis Methods in Physical Oceanography.* 2nd ed. Elsevier, 638 pp.

Fer, I., 2009: Weak vertical diffusion allows maintenance of cold halocline in the central Arctic. *Atmos. Oceanic Sci. Lett.,* **2,** 148–152.

——, R. Skogseth, and F. Geyer, 2010: Internal waves and mixing in the marginal ice zone near the Yermak Plateau. *J. Phys. Oceanogr.,* **40,** 1613–1630, doi:10.1175/2010JPO4371.1.

Furuichi, N., T. Hibiya, and Y. Niwa, 2008: Model-predicted distribution of wind-induced internal wave energy in the world's oceans. *J. Geophys. Res.,* **113,** C09034, doi:10.1029/2008JC004768.

Garrett, C. J., and W. H. Munk, 1975: Space-time scales of internal waves: A progress report. *J. Geophys. Res.,* **80,** 291–297, doi:10.1029/JC080i003p00291.

Gregg, M. C., E. A. D'Asaro, T. J. Shay, and N. Larson, 1986: Observations of persistent mixing and near-inertial internal waves. *J. Phys. Oceanogr.,* **16,** 856–884, doi:10.1175/1520-0485(1986)016<0856:OOPMAN>2.0.CO;2.

Guthrie, J., J. H. Morison, and I. Fer, 2013: Revisiting internal waves and mixing in the Arctic Ocean. *J. Geophys. Res.,* **118,** 3966–3977, doi:10.1002/jgrc.20294.

Halle, C., and R. Pinkel, 2003: Internal wave variability in the Beaufort Sea during the winter of 1993/1994. *J. Geophys. Res.,* **108,** 3210, doi:10.1029/2000JC000703.

Kwok, R., and D. A. Rothrock, 2009: Decline in Arctic sea ice thickness from submarine and ICESat records: 1958–2008. *Geophys. Res. Lett.,* **36,** L15501, doi:10.1029/2009GL039035.

Leaman, K. D., and T. B. Sanford, 1975: Vertical energy propagation of inertial waves: A vector spectral analysis of velocity profiles. *J. Geophys. Res.,* **80,** 1975–1978, doi:10.1029/JC080i015p01975.

Lee, D.-K., and P. P. Niiler, 1998: The inertial chimney: The near-inertial energy drainage from the ocean surface to the deep layer. *J. Geophys. Res.,* **103,** 7579–7591, doi:10.1029/97JC03200.

Levine, M. D., C. A. Paulson, and J. H. Morison, 1985: Internal waves in the Arctic Ocean: Comparison with lower-latitude observations. *J. Phys. Oceanogr.,* **15,** 800–809, doi:10.1175/1520-0485(1985)015<0800:IWITAO>2.0.CO;2.

——, A. P. Clayton, and J. H. Morison, 1987: Observations of internal gravity waves under the Arctic pack ice. *J. Geophys. Res.,* **92,** 779–782, doi:10.1029/JC092iC01p00779.

McPhee, M. G., 2008: *Air-Ice-Ocean Interaction: Turbulent Ocean Boundary Layer Exchange Processes.* Springer, 215 pp.

——, T. Kikuchi, J. H. Morison, and T. P. Stanton, 2003: Ocean-to-ice heat flux at the North Pole environmental observatory. *Geophys. Res. Lett.,* **30,** 2274, doi:10.1029/2003GL018580.

Merrifield, M. A., and R. Pinkel, 1996: Inertial currents in the Beaufort Sea: Observations of response to wind and shear. *J. Geophys. Res.,* **101,** 6577–6590, doi:10.1029/95JC03625.

Morison, J. H., C. E. Long, and M. D. Levine, 1985: Internal wave dissipation under sea ice. *J. Geophys. Res.,* **90,** 11 959–11 966, doi:10.1029/JC090iC06p11959.

Osborn, T. R., 1980: Estimates of the local rate of vertical diffusion from dissipation measurements. *J. Phys. Oceanogr.,* **10,** 83–89, doi:10.1175/1520-0485(1980)010<0083:EOTLRO>2.0.CO;2.

Pinkel, R., 1984: Doppler sonar observations of internal waves: The wavenumber-frequency spectrum. *J. Phys. Oceanogr.,* **14,** 1249–1270, doi:10.1175/1520-0485(1984)014<1249:DSOOIW>2.0.CO;2.

——, 2005: Near-inertial wave propagation in the western Arctic. *J. Phys. Oceanogr.,* **35,** 645–665, doi:10.1175/JPO2715.1.

——, 2008: The wavenumber–frequency spectrum of vortical and internal-wave shear in the western Arctic Ocean. *J. Phys. Oceanogr.,* **38,** 277–290, doi:10.1175/2006JPO3558.1.

Plueddemann, A. J., R. Krishfield, T. Takizawa, K. Hatakeyama, and S. Honjo, 1998: Upper ocean velocities in the Beaufort Gyre. *Geophys. Res. Lett.,* **25,** 183–186, doi:10.1029/97GL53638.

Polzin, K., E. Kunze, J. Hummon, and E. Firing, 2002: The finescale response of lowered ADCP velocity profiles. *J. Atmos. Oceanic Technol.,* **19,** 205–224, doi:10.1175/1520-0426(2002)019<0205:TFROLA>2.0.CO;2.

Rainville, L., and R. A. Woodgate, 2009: Observations of internal wave generation in the seasonally ice-free Arctic. *Geophys. Res. Lett.,* **36,** L23604, doi:10.1029/2009GL041291.

Sanford, T. B., E. A. D'Asaro, E. Kunze, J. H. Dunlap, R. G. Drever, M. A. Kennelly, M. D. Prater, and M. S. Horgan, 1993: An XCP user's guide and reference manual. Applied Physics Laboratory Tech. Rep. APL-UW TR9309, 120 pp.

Sirevaag, A., and I. Fer, 2012: Vertical heat transfer in the Arctic Ocean: The role of double-diffusive mixing. *J. Geophys. Res.,* **117,** C07010, doi:10.1029/2012JC007910.

Stroeve, J. C., V. Kattsov, A. Barrett, M. Serreze, T. Pavlova, M. Holland, and W. N. Meier, 2012: Trends in Arctic sea ice extent from CMIP5, CMIP3 and observations. *Geophys. Res. Lett.,* **39,** L16502, doi:10.1029/2012GL052676.

Turner, J. S., 2010: The melting of ice in the Arctic Ocean: The influence of double-diffusive transport of heat from below. *J. Phys. Oceanogr.,* **40,** 249–256, doi:10.1175/2009JPO4279.1.

Yamazaki, H., and T. Osborn, 1990: Dissipation estimates for stratified turbulence. *J. Geophys. Res.,* **95,** 9739–9744, doi:10.1029/JC095iC06p09739.